High resolution infrared thermography for capturing wildland fire behavior-RxCADRE 2012

Journal:	*International Journal of Wildland Fire*
Manuscript ID:	WF14165
Manuscript Type:	Research Paper
Date Submitted by the Author:	13-Sep-2014
Complete List of Authors:	OBrien, Joseph; US Forest Service, Center for Forest Disturbance Science Loudermilk, Eva (Louise); USDA Forest Service, Center for Forest Disturbance Science Hornsby, Benjamin; US Forest Service, Center for Forest Disturbance Science Hudak, Andrew; USDA Forest Service, Rocky Mountain Research Station Bright, Benjamin; USDA Forest Service, Rocky Mountain Research Station Dickinson, Matthew; USDA Forest Service, Northern Research Station Hiers, John; Eglin Air Force Base, Natural Resources Management Teske, Casey; University of Montana, Center for Landscape Fire Analysis Ottmar, Roger; USDA Forest Service, Pacific Northwest Research Station
Keyword:	Fire behaviour, Fire intensity, Instrumentation, Remote sensing, Scale: local

High resolution infrared thermography for capturing wildland fire behavior—RxCADRE 2012

Joseph O'Brien[A,G] *E. Louise Loudermilk*[A], *Benjamin Hornsby*[A], *Andrew T. Hudak*[B], *Benjamin C. Bright*[B], *Matthew B. Dickinson*[C], *J. Kevin Hiers*[D], Casey Teske[E] and *Roger D. Ottmar*[F]

[A]US Forest Service, Center for Forest Disturbance Science, Southern Research Center, 320 Green St., Athens, GA 30602, USA

[B]US Forest Service Rocky Mountain Research Station, Forestry Sciences Laboratory, 1221 South Main Street, Moscow, ID 83843, USA

[C]US Forest Service, Northern Research Station, 359 Main Road, Delaware, OH 43015, USA

[D]Wildland Fire Center, Eglin Air Force Base, 107 Highway 85 North, Niceville, FL 32578, USA

[E]University of Montana, FireCenter, Room 441, Charles H. Clapp Building, Missoula, MT 59812, USA

[F]US Forest Service, Pacific Northwest Research Station, Pacific Wildland Fire Sciences Laboratory, 400 North 34th Street, Suite 201, Seattle, WA 98103, USA

[G]Corresponding author. Email: jjobrien@fs.fed.us

Abstract

Wildland fire radiant energy emission is one of the only measurements of combustion that can be made at wide spatial extents and high temporal and spatial resolutions. Furthermore, spatially- and temporally-explicit measurements are critical for making inferences about fire effects and useful for examining patterns of fire spread. In this manuscript we describe our methods for capturing and analyzing spatially and temporally explicit longwave infrared (LWIR) imagery developed through the RxCADRE (Prescribed Fire Combustion and Atmospheric Dynamics Research Experiment) project and its utility in investigating fire behavior and effects. We compare LWIR imagery captured at fine (1 to 4 cm^2) and moderate (1 m^2) resolutions and temporal resolution from 0.25 to 1 Hz using both nadir and oblique measurements. We analyze fine-scale spatial heterogeneity of fire radiant power and energy released in several experimental burns. There was concurrence between the measurement strategies although the oblique view estimates of fire radiative power were consistently higher than the nadir view estimates. The nadir measurements illustrate the significance of fuel characteristics, particularly type and connectivity in driving spatial variability at fine-scales. Spatially and temporally resolved data from these techniques show promise to effectively link the combustion environment with post-fire processes, remote sensing at larger scales, and wildland fire modeling efforts.

Summary

We describe the utility of LWIR imagery for capturing fire behavior in space and time. We explore how images captured at different perspectives and varying spatial resolutions affect measurements of fire. We discuss of the utility of multiple measurements and potential in quantifying fire patterns of fire spread and fire effects.

Introduction

Measuring wildland fire is inherently difficult, especially relative to understanding the ecological effects of fire. For many years, the technology available for measuring wildland fire intensity was limited to qualitative descriptions, visual estimates, point measurements, or relative indices of intensity (Kennard et al. 2005). This hindered the ability to accurately capture fire in ways that could mechanistically link fire behavior (energy release) with fire effects (energy transfer), especially in a spatial manner. Direct measurements of energy transfer are critical for predicting and understanding both first- and second-order fire effects (Van Wagner 1971; Johnson and Miyanishi 2001, Dickinson and Ryan 2010). Recent advances in technology have made it possible to measure the fire energy environment across time and space using infrared thermography. Long wave infrared (LWIR) thermography is a well-established measurement technique (Maldague 2001; Melendez et al 2010) that is especially useful because the long wave portion of the infrared spectrum is most sensitive to radiation emitted by surfaces heated by fire such as fuels, plants, woodland creatures, and soils. Furthermore, the system can have high spatial and temporal resolution and does not require sensor contact with the object being measured. LWIR thermography is especially useful for fire effects research since the LWIR radiation emitted by an object represents the integrated effect of radiative, convective, and conductive heating impinging on the object of interest. The system used in the research reported here employed a focal plane array designed to detect LWIR, a band especially useful for smoky environments because part of the bandpass is minimally affected by fine particulates, hot gas emissions and infrared absorption by gases (Rogalski and Chrzanowski 2001) See Loudermilk et al. (2012) and Rogalski and Chzanowski (2002) for details on the principles, benefits, and limitations of LWIR thermography.

The data recorded by LWIR thermography is spatially explicit and examining the spatial dependencies or autocorrelation of the fire radiation environment can be useful in many ways. First, one can de-couple the spatial trends to better understand the underlying mechanisms that either drive fire behavior (e.g. fuel type and arrangement) or how fire behavior influences subsequent fire effects (Hiers *et al.* 2009; Loudermilk *et al.* 2009, 2012) These spatial trends can also be used to evaluate fire spread models (e.g. Berjak and Hearne 2002; Achtemeier *et al.* 2012) created for similar systems to determine if they capture the appropriate scale of variability measured in the field. A spatio-temporal analysis could be performed using simultaneously recorded wind data (e.g. with anemometers, Butler *et al.* this issue) to isolate direct wind effects from other fire behavior characteristics that may be useful for uncovering the mechanisms driving wildland fire spread.

In this manuscript we describe our methods for capturing and analyzing spatially and temporally explicit LWIR temperature data developed through the RxCADRE (Prescribed Fire Combustion and Atmospheric Dynamics Research Experiment) project and its utility in investigating fire behavior and effects. We compare LWIR data captured at fine (1–4 cm^2) and moderate (1 m^2) resolutions and analyze fine-scale spatial heterogeneity of fire radiant power and energy released in several experimental burns.

Methods

For details on the site and experimental design, see Ottmar et al. this issue.

LWIR thermography measurements

We employed two measurement strategies to capture thermal data at fine (1–4 cm^2) and moderate (1 m^2) resolutions. The fine scale measurements were captured using an 8.2-m tall tripod (Fig. 1*a*) designed to provide a nadir perspective and the moderate scale resolution data were collected at an oblique angle from a 25.9-m boom lift (Fig. 1*b*). The nadir views were positioned over pre-surveyed 4 x 4 m super-highly instrumented plots (SHIPs) located randomly in each 20 m x 20 m highly instrumented plot (HIP) (see Ottmar et al. this issue). The SHIPs had 100-cm^2 square steel plates placed at 1-m intervals around the plot perimeter as "cold targets" (Fig. 2). The low emissivity (ε) of the steel made them easily detectable in the thermal image and useful for geo-referencing and cropping the plots. The boom lift was located 10 to 25 m from the control lines demarcating the small units and positioned at the center of and perpendicular to the ignition line upwind of the units in all cases with the exception of S9. Locating the boom lift upwind lessened the likelihood of unburned fuels obscuring the LWIR signal from the fire, and being unobscured by smoke provided an additional measure of safety around unmanned aerial systems. For both the nadir and oblique viewing LWIR cameras, an image of the ambient temperature range (0–300°C) was collected just before ignition.

The tripod system consisted of an equilateral triangular aluminum plate with 1 m sides positioned 8.2 m above the ground by three 3.175-cm diameter American National Standards Institute (ANSI) schedule 40 pipe legs. The legs consisted of four sections (three aluminum, the lowest steel) connected by ferrules locked in place with D-rings and were attached to each apex of the triangular plate by an axle allowing the legs to swivel in two dimensions. Steel was used for the lowest section due to its high melting point and high density that increased tripod stability. The LWIR camera was mounted inside a metal ammunition box (emptied of ammunition) with ports cut for optics and cabling that was raised to the bottom of the triangular plate via a 9.5-mm braided steel cable and winch. Cabling, if present, was armored by 2.5-cm diameter flexible aluminum conduit.

The LWIR optics were positioned 7.7 m above the center of the small plots. For the nadir measurements, we used three thermal imaging systems from FLIR Inc.: the SC660, S60 and T640. The oblique imagery was collected with the SC660. The height of the tripod system provided a 4.8 m x 6.4 m field of view for the SC660 and S60, and 2.5 m x 3.3 m field of view for the T640. The field of view of the oblique imagery covered most of the area of the small burn blocks and captured the entire fire perimeter from ignition until the fire passed the central instrument cluster and/or reached the downwind control line. The SC660 and T640 focal-plane arrays have a resolution of 640 x 480 pixels while the S60 has a resolution of 320 x 240 pixels. The SC660 and T640 have a sensitivity of 0.03°C while the S60 has a sensitivity of 0.06°C. All systems have a spatial resolution of 1.3 mRad and a thermal accuracy of ± 2%. Data were captured at 1 Hz with the SC660 and T640 and 0.25 Hz for the S60. Emissivity was set at 0.98 and the air temperature and relative humidity were noted for postprocessing. The temperature range for all cameras during the fires was set to 300–1500°C for collecting active fire LWIR data. High-definition digital visual imagery was collected before and during the fire from video cameras located adjacent to the LWIR cameras.

Image processing

The FLIR systems gave radiometric temperatures in °C as raw output. For all LWIR imagery, the native file format was converted to an ASCII array of temperatures in °K with rows and columns representing pixel positions. For the nadir plots, we then extracted the area of interest using Python 2.7 programming language. The selected array of temperatures was converted into another ASCII file of three columns where x,y,z = pixel row, pixel column, and temperature. Temperatures were then converted into W m^{-2} (fire radiated flux density) (FRFD) using the Stefan-Boltzmann equation for a gray body emitter. Again, ε was assumed to be 0.98. We also calculated mean residence time as the average amount of time a pixel was measured to be >525°C (Draper point) among all pixels in the burn block for the duration of the event and maximum residence time was the maximum number of times a single pixel was measured to be >525°C. Our technique likely underestimates the contribution of flames to power and energy release because of low flame ε (Johnson et al. 2014) and flames whose peak emissions are in the midwave infrared portion of the spectrum, but does accurately capture temperatures of the burning fuel and heated soil.

For the oblique platform, images were processed using Python 2.7 programming language and rectified using GDAL (2014). The image radiometric (effective) temperature values were converted to RGB values in a TIFF file for processing. This entailed converting temperature values into three bands restricted to 256 values. All temperature values were converted to integers. The red band preserved the hundreds and thousands place of the temperature values, while the blue band preserved the one to tens place of the temperature values of each temperature value. All green band pixel values were zero (no conversion). The red band pixel values were calculated using the temperature (T) pixel values in the following equation, with conversions to integer (int): ((T/10)int ×1.7)int. The blue band was calculated by the following equation:

$$(T_{int} \times 10-(T/10)_{int} \times 100) \times 2$$

Twelve ground control points for each small burn block were identified using surveyed positions of hot targets (e.g. charcoal cans), instruments, and ignition points. The prefire LWIR image was critical for identifying ground control points because any surveyed instruments with low ε (e.g. tripod, radiometer, or any steep instrument enclosures), any obvious ground features (e.g. vegetation or permanent infrastructure), and surveyed hot targets were only visible in this pre-fire image (Fig. A1). LWIR images of the initial ignition point and ends of ignition lines (Fig. A2), which were surveyed, provided three ground control points. In the end, only the first few images (pre-fire, ignition points) were used for identifying the ground control points. As such, we assumed that the remaining images had the same coordinate frame (i.e. no camera movement). In reality, there was some camera movement, the degree of which was determined by wind conditions. Although this may have intermittently introduced an element of spatial error in the images, the coincidence of the measurements was tested against the nadir images (see below) and showed concordance. Within GDAL (2014), each image was rectified using a third-order polynomial (using the 12 control points), bilinear resampling, and the EPSG projection 26916 (NAD 83/UTM zone 16N) with an output resolution of 1 m x 1 m. Once rectified, each image was converted back to radiometric temperature values by back-calculating using the previous equations, and estimates of fire radiative power (FRP) by pixel were calculated using the Stefan-Boltzmann Law for a grey body emitter. Fire pixel values were summed across units at each time step to give whole fire total fire radiative energy (FRE) (Table 1).

Total fire radiative energy density (FRED) was calculated across oblique LWIR images (Fig. 3). To calculate FRED on a pixel-by-pixel basis, we reduced the geo-registration differences between consecutive images that were caused by camera movement. This was done by resampling images (nearest neighbor) to a common origin and extent using Environment for Visualizing Images (ENVI) software. A total FRED image was created using the following:

$$FRED = 10^{-5} \times \sum_{i=2}^{n} 0.5 \times (FRFD_i + FRFD_{i-1}) \times (t_i - t_{i-1}) \quad \text{(Eqn. 1)}$$

where FRED is total fire radiative energy density (GJ ha^{-1}), *i* indicates time step, and *t* is the measurement frequency (s) (Fig. 3). Image processing was done using the raster package (Hijmans 2013) in R (R Core Team 2013).

The FRED images (Fig.3) illustrate the area recorded by the oblique LWIR camera, where the LWIR camera was turned off before the fire was complete. Fig. 3 also illustrates the distortion caused by the oblique angle and camera movement that was not accounted for during the rectification process.

To assess potential measurement error in long-range oblique LWIR measurements, we compared spatially coincident oblique and nadir LWIR estimates of FRP and FRE. Nadir LWIR measurements over a field of view that ranged from 12 to 16 m^2 were made within a single 4 m x 4 m SHIPs within each of four small burn blocks (S5, S7, S8, S9) (Table 2). The distance between the oblique LWIR camera and the nadir LWIR camera field of view ranged from 125 to 230 m. All inclusive pixels within the 12- to 16-m^2 area (see Table 2) were used for the nadir LWIR (about 6,400 pixels m^{-2}). As the oblique LWIR (1 m^2) imagery pixels did not overlap perfectly within the nadir LWIR camera's area, all fully and partially overlapping pixels from the oblique LWIR imagery were used in a bootstrapping technique to estimate a mean and standard deviation of FRP across pixels and images. For example, in each oblique LWIR image in S5 (within the 12-m^2 nadir area field of view) (Table 2), 20 overlapping oblique LWIR image pixels were stored as a sample population of LWIR data. We used bootstrapping, sampling 12 pixels with replacement 50 times. From this, we calculated a mean and standard deviation of FRP for each image. FRP flux density was the FRP divided by the (12 m^2) area. Total FRE (Table 2) for the oblique imagery is the total 'mean' FRP values from bootstrapping.

Spatial and temporal pattern

We chose, as examples, one nonforested (S5) and one forested (L2F HIP3) SHIP to examine the fine-scale spatial heterogeneity of fire behavior. These plots were chosen for comparison because they had considerable differences in fuel loadings (Ottmar et al. *this issue*) and overstory influence (no canopy vs. canopy) and were quality, high sample frequency datasets (collected at 1 Hz). We tested for and modeled the spatial dependencies (autocorrelation) within each plot. Moran's I was calculated using the Analyses of Phylogenetics and Evolution ('ape' v 3.0-10) library package in the R programming language v 3.0.1 (R Core Team 2013) to test for spatial autocorrelation. To assess the range of spatial correlation and magnitude of spatial variability of energy released (J) and residence time (s) within plots, we modeled the semivariance (spatial autocorrelation function) using the geostatistics data analysis (geoR v 1.7-4) and statistical data analysis (StatDA v 1.6.7) library packages in R. An isotropic exponential autocorrelation function (Goovaerts 1997) was fit to the empirical semivariance, with a maximum range of 2 m (about 1/2 plot distance). An individual nugget parameter was fit to each model, while sill and range parameters were automated within R.

Temporal autocorrelation and its confidence interval were determined for each time series of whole-fire FRP derived from oblique LWIR imagery of small burn blocks. Autocorrelation and confidence intervals (95%) were determined using SAS 9.4 PROC TIMESERIES (SAS Institute Inc. 2013). Significant autocorrelation was determined if the autocorrelation for a given lag was less than 1.96 standard deviations from zero (i.e. 95% confidence interval). The longest significant lag is reported.

Results

A comparison of LWIR and visual imagery shows that the LWIR imagery captures a broader range of the combustion environment (both smoldering and flaming phases) whereas only the flaming phase of combustion was apparent in the visual images (Fig. 2). Both the nadir and oblique (rectified) LWIR imagery illustrated fluctuations in FRP influenced by fuels and changing wind patterns at the flaming front at both fine (Fig. 4, 5) and moderate (Fig. 6) scales. These data reflect the heterogeneity of FRP that was released from these surface fires. This was shown in the nadir LWIR imagery (e.g. Fig. 2a), where detailed fire line intensity was highly variable within a small area (about 16 m^2). This also was evident in the oblique LWIR imagery (Fig. 7), where fire line geometry and shifting wind patterns influenced fireline depth (e.g. backing vs. flanking fire) and total FRED across the burn block (Fig. 3). As the fireline depth was often within 2 m, the nadir LWIR camera was able to record FRP of the true flaming front, without the signal attenuation that may be caused by blending burning and non-burning areas within pixels at coarser scales.

In the oblique LWIR imagery, total FRE ranged from 1.3 to 5.9 GJ within 0.5–2.31 ha burned within the six small nonforested plots (Table 1). Mean FRED ranged from 1.2 to 3.9 GJ ha^{-1}. Mean and maximum FRP ranged from 1.2 to 5.1 MW and 5.5 to 41.7 MW. The mean active flaming area (number of pixels) across images ranged from 88 to 353 m^2, with considerable variation within each fire (standard deviation: 86–356 m^2). In the nadir LWIR imagery, total FRE ranged from 1.2 to 12.1 MJ, within a 4 to 16 m^2 plot area in the ten plots (Table 2). Mean and maximum FRP ranged from 14 to 41 kW and 70 to 208 kW. Mean and maximum FRP flux density ranged from 1.3 to 3.7 and 5.5 to 20.9 kW m^{-2}. Mean and max FRP as well as mean FRP flux density between the oblique and nadir LWIR imagery were similar, but consistently higher in the oblique LWIR estimates across plots (except for max FRP flux density in S9) (Fig. 8, 9)

(Table 2) though we were unable to test the significance due to the lack of replication. We were unable to compare between the oblique and nadir LWIR data in S7 because we could not ensure proper spatial overlap of the two instruments due to movement of the oblique view camera when the fire passed through the nadir plot. The comparison of maximum power among the techniques may be misleading due to the high frequency fluctuations of peak fire power that are underestimated when sampling at frequencies less than approximately 100 Hz, although integrated measurements are less affected even with sampling frequencies of 1 Hz (Frankman et al. 2013). Total FRE from the oblique LWIR data was comparable to the nadir LWIR data, but had mixed results (Table 2). For instance, the oblique FRE estimates were lower for S5 (2.1 (s.d. 0.6) vs. 3.2 MJ), higher for S8 (2.0 (s.d. 0.6) vs. 1.2 MJ), and very similar for S9 (1.3 (s.d. 0.3) vs. 1.4 MJ) than nadir estimates.

Spatial and temporal pattern

The comparison between two SHIPs, L2F HIP 3 (forested), and S5 (nonforested) displayed heterogeneity in FRE (Fig. 10), though the scales differed in both space and time. Both SHIPs illustrated significant ($p<0.05$) positive spatial autocorrelation of energy released and residence time, and the range (distance) of spatial variability among SHIPs were within 1 m. The difference between SHIPs were noted by the magnitude of spatial variability (i.e., partial sill) between SHIPs (Fig. 11). Total FRE was 3.2 MJ and 12.1 MJ for the nonforested and forested SHIPs, respectively. Mean (standard deviation) residence time was 20 (16) s and 44 (44) s for the nonforested and forested plot, respectively. Maximum residence time was 96 s and 672 s for the nonforested and forested plot, respectively.

The time-series analysis showed that whole-fire FRP for small burn blocks (N = 6) was significantly autocorrelated to an average of 1.2 minutes. The range in longest significant lag was 0.9 to 1.6 min and the standard deviation was 0.4 min.

Discussion

Precise measurements at multiple scales in space and time were key for capturing and understanding the variability associated with our experimental fires. We observed the expected variation in FRE and FRP between different fuels types (forested vs. nonforested units) but also detected a large amount of variation within fuel types. This variation was evident over multiple scales, despite the relatively homogeneous vegetation of managed grassy fields and prescribed fires lit under similar conditions. For example, from the oblique LWIR imagery in the six small burn blocks, mean FRP ranged from 1.2 to 5.1 MW and the maximum FRP ranged from 5.5 to 41.7 MW across plots, while mean FRED ranged between 1.2 and 3.9 GJ ha^{-1}across burn blocks (Fig. 3).

Our techniques for employing LWIR thermal imagers allowed us to collect precise fine (1-4 cm^2) and moderate (1 m^2) resolution fire behavior from both nadir and oblique angles. We found a promising coincidence of measurements of FRP and total FRE between the two instruments from the two perspectives. The rectification process generated comparable FRP and total FRE between oblique-viewing and nadir-viewing LWIR cameras (Table 2) (Figs. 8, 9). These data and relationships across scales are just beginning to be explored quantitatively. Although the nadir LWIR imagery has been quantified and analyzed previously for surface fires (Hiers et al. 2009; Loudermilk et al. 2012), the oblique LWIR data were novel. Here, we were able to exploit

LWIR data across a 2-ha area to provide georeferenced FRFD of a moving surface fire at 1 Hz over the entire fire perimeter throughout the 20-30 min. prescribed burns (e.g. Fig. 7).

Although total FRE from the oblique LWIR imagery was variable (see Table 2) when compared to the nadir imagery within the 12–16 m^2 areas of coincidence (Fig. 8*c*), the results were similar even given the difference in spatial resolution between the instruments (1 m^2 vs. ~4 cm^2). We could not definitively identify the cause of the discrepancies between the measurements, but we can infer that camera movement, absorption of radiant energy by intervening atmosphere, pixel distortion caused by the rectification process, and the distance of the plot from the oblique instrument platform were likely responsible for differences we observed. For example, the total FRE of the oblique LWIR imagery was higher than the nadir for S8 [2.0 (0.6) vs. 1.2 MJ] likely because of the camera movement we saw in the video sequences. This would result in commission errors from pixels outside the nadir plot. In another instance, total FRE was lower in S5 for the oblique data [2.1 (0.6) vs. 3.2 MJ], likely due to signal attenuation narrowing the power distribution curve (Fig. 8*a*). Total FRE was most comparable for S9 [oblique vs. nadir: 1.3(0.3) vs. 1.4 MJ], where the entire curve of FRP was captured by both instruments (Fig. 9*b*) because the nadir plot was comparatively stable and closer to the oblique view platform (125 m for S9 vs. 190 for S5 and 230 for S8). Nevertheless, as the oblique LWIR imagery was collected at lower angles and greater distances (125–230 m) than the nadir LWIR imagery, these measurements were more susceptible to the aforementioned errors. Because the nadir camera was securely positioned directly above the fire and less than 8 m from the ground, errors of distortion or omission and commission were minimal.

Signal attenuation in the oblique views was likely an important source of error as pixels included both burning and nonburning areas that would tend to reduce the average radiometric temperature and, given the fourth-power dependency between temperature and FRFD through the Stefan-Boltzmann equation, attenuating the signal emanating from the fire line. From this, we concluded that if the imager has a minimum resolution greater than the maximum fire line depth, fire radiative power within pixels can be underestimated, a common issue with more coarse scale remote sensing of FRP. For example, in S5, we can see from the nadir LWIR images (data not shown, but see Fig. 2 for example) that the fire line depth was less than 2 m. The 1 m^2 pixels of the oblique LWIR imagery were integrating radiation from both burning and non-burning areas, creating opportunities for errors of omission as the fire enters and leaves the plot (see tails of distribution of FRP) (Fig. 7*a*, 8*b*). Even with these discrepancies, the similarities in FRE slopes (Fig. 8*c*) between the two LWIR systems illustrated that overall fire behavior dynamics were captured accurately by the oblique LWIR imagery. Furthermore, the oblique LWIR image overlay of the total area sampled (Fig. 3) was successful, and allowed for cross-platform comparisons (See Hudak et al. *this issue* and Dickinson et al. *this issue*). This also provides opportunities for further analysis with spatial fuels (from terrestrial LIDAR, e.g. Loudermilk et al. 2009, Seilestad et al. *this issue*) and influential weather characteristics, such as wind patterns from anemometers (e.g. Butler et al. *this issue*) to analyze their relative contribution through space and time. Furthermore, both the nadir and oblique FLIR data provide valuable ground truth for validating complementary infrared-based measurements from airborne (Hudak et al. *this issue*) and spaceborne platforms (Dickinson et al. *this issue*).

The oblique platform was not effective in the large forested unit of this study, mainly due to canopy obstructing the view of the surface fire. Using the oblique approach would be most effective when deployed under a tree canopy or in shrublands and grasslands. Although the signal obstruction within the nonforested plots was not quantified, they were likely minimal as the fuels were of low stature and relatively sparse. The one oblique camera (S9) positioned in front of the moving fire, where obstruction by unburned fuels was most likely still resulted in similar estimates of FRP and total FRE compared to at nadir (Table 2). To reduce potential radiation obstruction, we recommend positioning the imaging system upwind of head fires that would remove fuels in the optical path of the camera.

Spatial and temporal autocorrelation

The spatial variability of fire behavior within and among plots can be influenced by many factors, such as fuel loading and type, fuel structure including fuel continuity, and local weather (wind, ambient temperature, and relative humidity). In this study, we found that although the FRE was almost quadruple in the forested plot compared to the nonforested plot (12.1 vs. 3.2 MJ), the spatial variability of FRP was lower in the forested plot (Fig. 11). This is likely due to the connectivity of fuels (pine litter and grasses) within this forested plot which may not be representative of the entire L2F block (See Hudak et al. *this issue*), compared to the patchiness (bare soil and grass clumps) in the nonforested plot (Fig. 10). In contrast, the spatial variability of residence time was higher in the forested plot. This was likely due to smoldering of downed woody debris found within the forested plot (See Ottmar et al. *this issue*), compared with the quick ignition potential and rapid consumption of grasses in the nonforested plot. These results are consistent with previous work, where we found that heterogeneity in similar frequent low-intensity fires was driven by fuel type and fuel structure (Loudermilk et al. 2012), and less by fuel loadings. Moreover, the abundance of pine litter may be a factor as well. There was essentially no pine litter in the nonforested plot (Ottmar et al. *this issue*), reducing both fuel continuity and energy potential (Fonda and Varner 2004).

In future studies, infrared imagery with comparable spatial and temporal resolution and extent will likely be valuable in understanding the relative role of fuels and wind fields on fire radiant emissions and fire spread. Temporal autocorrelation was observed to 1.2 min on average, information that, in future work, can be related to coincident meteorological measurements. The 1.2-min temporal autocorrelation would appear to be largely dependent on wind gusts and shifts, though fuel variability may also have played a role (see Sielestad et al. *this issue*).

Fire behavior, scale, and fire effects

This study also supports the potential for fine scale measurements to link fire behavior and fire effects. For example, in longleaf pine forests, plant-plant interactions that make-up the diverse understory are driven not only by frequent fire (Kirkman et al. 2004) but by fine-scale heterogeneity of fuels that are determined by the tree canopy (Mitchell et al. 2006). Trees provide both the pine litter that promotes fire spread, and pine cones that alter fine-scale fire intensity and severity. For instance, there is evidence that legume mortality occurs under burning pine-cones creating fine-scale recruitment sites (Wiggers et al. 2013). Research is currently underway to identify and quantify fine-scale fire effects that may determine understory plant community assembly. From the moderate scale fire behavior data (oblique LWIR imagery), we can identify coarser scale fire patchiness likely related to similar scale vegetation patterns.

Considerations for LWIR imagery measurements

There are several considerations that are important when collecting and analyzing LWIR thermographic measurements. Camera stability is critical since image georeferencing, cropping, and rectification all depend on initial LWIR images (e.g. pre-fire ‘cold’ image) (Fig. A1), ignition points) that were used for locating the ground control points. In our processing approach, all remaining images were assumed to have the same coordinate frame; thus any camera movement would introduce error in the form of noise or potential bias. Identifying an object in the LWIR requires that it be either warmer or cooler or have a different ε than the surroundings. The deployment of targets detectable at the imager temperature scales required for measuring fire would allow frame by frame rectification. Unfortunately, very hot targets are difficult to deploy and potentially dangerous. If the imager platform is stable, the difficulties associated with hot targets can be mitigated by using markers made of low ε materials reflective materials. These materials with an ε less than 0.3 appear dramatically colder than the surrounding high ε soil and vegetation. These cold targets worked especially well for the nadir measurements. Hot targets (e.g. charcoal canisters) were especially effective for the oblique rectification process as they were more apparent at greater distances, although reflective low ε instrument enclosures and other permanent structures were also useful as control points. In images with active fire, control points were difficult to see and were often invisible (Fig. A1). As such, the pre-fire image of ambient conditions was critical for identifying the control points.

Conclusions

LWIR imagery at multiple scales offers an opportunity to effectively link the combustion environment with post-fire processes, remote sensing at larger scales, and wildland fire modeling efforts. Precise measurements at multiple scales in space and time were key for capturing and understanding the variability associated with our experimental fires. These kinds of data will be critical for the development and evaluation of new fire behavior models that incorporate both stochastic and mechanistic processes that occur across scales. The accurate two dimensional spatial measurements of surface radiative energy release over time can connect fire to such processes as soil heating, plant mortality, and tissue damage and also provide valuable data on fire spread and radiant energy fluxes useful for refining fire spread and smoke dynamics models (e.g. Achtemeier et al. 2012; Atchemeier 2013).

Acknowledgements

This research was funded primarily by the Joint Fire Science Program (Project #11-2-1-11) with additional support from the Strategic Environmental Research and Development Program (#RC-398 2243). Brett Williams of the Jackson Guard Wildland Fire Center went above and beyond the call of duty as incident commander. We thank all the Jackson Guard wildland fire personnel as the success of RxCADRE depended on their skill and professionalism. We thank Mac Callaham, Christie Stegall, Dexter Strother and Evelyn Wenk of the USDA Forest Service, who were invaluable in the field.

References

Achtemeier GL (2013) Field validation of a free-agent cellular automata model of fire spread with fire–atmosphere coupling. *International Journal of Wildland Fire* **22**, 148–156. doi: 10.1071/WF11055

Achtemeier GL, Goodrick SA, Liu Y (2012) Modeling multiple-core updraft plume rise for an aerial ignition prescribed burn by coupling Daysmoke with a cellular automata fire model. *Atmosphere* **3**, 352–376. doi: 10.3390/atmos3030352

Berjak SG, Hearne, JW (2002) An improved cellular automaton model for simulating fire in a spatially heterogeneous savanna system. *Ecological Modelling* **148**, 133–151. doi: 10.1016/S0304(01)00423-9

Dickinson MB, Ryan KC (2010) Introduction: strengthening the foundation of wildland fire effects prediction for research and management. *Fire Ecology* **6**, 1–12. doi: 10.4996/fireecology.0601001

Fonda, R Varner J (2004) Burning characteristics of cones from eight pine species. *Northwest Science* **78**, 322–333.

Frankman D, Webb BW, Butler BW, Jimenez D, Harrington M (2013) The effect of sampling rate on interpretation of the temporal characteristics of radiative and convective heating in wildland flames. *International Journal of Wildland Fire* **22**, 168–173. doi: 10.1071/WF12034

GDL 2014. GDL—Geospatial Data Abstraction Library: version 1.10.1, Open Source Geospatial Foundation. http://gdal.osgeo.org. (10 August 2014)

Goovaerts P (1997) 'Geostatistics for natural resources evaluation.' (Oxford University Press: New York)

Hiers JK, O'Brien JJ, Mitchell RJ, Grego JM, Loudermilk EL (2009) The wildland fuel cell concept: an approach to characterize fine-scale variation in fuels and fire in frequently burned longleaf pine forests. *International Journal of Wildland Fire* **18**, 315–325. doi: 10.1071/WF08084

Johnson, EA, Miyanishi, K (2001) 'Forest fires: behavior and ecological effects.' (Academic Press San Diego, CA)

Johnston J, Wooster M, Lynham T (2014) Experimental confirmation of the MWIR and LWIR grey body assumption for vegetation fire flame emissivity. *International Journal of Wildland Fire* **23**, 463–479. doi:10.1071/WF12197

Kennard DK, Outcalt KW, Jones D, O'Brien JJ (2005) Comparing techniques for estimating flame temperature of prescribed fires. *Fire Ecology* **1**, 75–84. doi: 10.4996/fireecology.010175

Kirkman LK, Goebel PC, Palik BJ, West LT (2004) Predicting plant species diversity in a longleaf pine landscape. *Ecoscience* **11**, 80–93.

Loudermilk EL, Hiers JK, O'Brien JJ, Mitchel, RJ, Singhania A, Fernandez JC, Cropper WP, Jr., Slatton KC (2009) Ground-based LIDAR: a novel approach to quantify fine-scale fuelbed characteristics. *International Journal of Wildland Fire* **18**, 676–685. doi: 10.1071/WF07138

Loudermilk EL, O'Brien JJ, Mitchell RJ, Cropper WP, Hiers JK, Grunwald S, Grego J, Fernandez-Diaz JC (2012) Linking complex forest fuel structure and fire behaviour at fine scales. *International Journal of Wildland Fire* **21**, 882–893. doi: 10.1071/WF10116

Maldague, X (2001) 'Theory and practice of infrared technology for nondestructive testing.' (Wiley: New York)

Melendez J, Foronda A, Aranda JM, Lopez F, Lopez del Cerro FJ (2010) Infrared thermography of solid surfaces in a fire. *Measurement Science and Technology* **21**, 105504. doi:10.1088/0957-0233/21/10/105504

Mitchell RJ, Hiers JK, O'Brien JJ, Jack S, Engstrom R (2006) Silviculture that sustains: the nexus between silviculture, frequent prescribed fire, and conservation of biodiversity in longleaf pine forests of the southeastern United States. *Canadian Journal of Forest Research* **36**, 2724–2736. doi: 10.1139/X06-100

R Core Team (2013) ' R: A language and environment for statistical computing.' (R Foundation for Statistical Computing: Vienna, Austria)

Rogalski A, Chrzanowski K (2002) Infrared detection and devices. *Opto-Electronics Review* **10**, 111–136.

SAS Institute Inc (2013) SAS® 9.4 (Cary, NC).

Van Wagner C (1971) Two solitudes in forest fire research. Canadian Forestry Service, Petawawa Forest Experiment Station, Information Report PS-X-29. (Chalk River, ON).

Wiggers MS, Kirkman LK, Boyd RS, Hiers JK (2013) Fine-scale variation in surface fire environment and legume germination in the longleaf pine ecosystem. *Forest Ecology and Management* **310**, 54–63. doi: 10.1016/j.foreco.2013.07.030

Table 1. **Details from oblique LWIR imagery, including fire radiative power estimates**

Oblique LWIR imagery had a resolution of 1m x 1m. Total area burned excludes unburned areas (pixels) within burn blocks. FRP = fire radiative power (across pixels). Total FRE = total fire radiative energy released from fire recorded in the burn block. Total area burned = mean number of 1-m^2 pixels burned at 1Hz (across LWIR images). FRED: Fire radiative energy density (GJ ha^{-1}).

Fire	Active flaming duration (min)	Mean (sd) active flaming area (m^2)	Total area burned (ha)	Total FRE (GJ)	Mean (SD) FRP (MW)	Max FRP (MW)	Mean (SD) FRED (GJ ha^{-1})
S3	26	324 (286)	2.16	5.7	4.2 (3.8)	15.4	3.0 (2.5)
S4	20	88 (86)	0.50	1.3	1.2 (1.4)	5.5	3.0 (2.5)
S5	29	289 (203)	1.14	5.9	3.9 (3.0)	14.0	3.9 (2.9)
S7	29	150 (217)	1.14	3.1	2.1(3.3)	18.8	3.0 (2.6)
S8	23	353 (356)	2.31	6.3	5.1 (6.7)	41.7	3.0 (3.1)
S9	17	177 (173)	1.82	1.9	2.0 (2.0)	7.8	1.2 (1.0)

Table 2. Radiative fire estimates from the nadir and oblique LWIR data within four small (S) nonforested burn blocks and three large (L) burn blocks. All FRP and FRE values from the oblique LWIR data were mean bootstrapped values of overlapping pixels within the nadir LWIR camera's field of view. Total FRE for the oblique LWIR imagery was the total mean FRP (total standard deviation FRP). See text in methods for details on bootstrapping. There were no usable oblique LWIR data collected at the large burn blocks, and S7 data within the overlap area was corrupted by camera movement. All blocks except L2F were nonforested.

	Block							
	S5		S7		S8		S9	
	Nadir	Oblique	Nadir	Oblique	Nadir	Oblique	Nadir	Oblique
Mean (SD) FRP (kW)	33 (32)	42 (32)	7 (9)	-	16 (28)	30 (26)	34 (47)	56 (40)
Max FRP (kW)	99	103	32	-	85	95	117	109
Mean FRP flux density (kW m^{-2})	2.8	3.6	0.4	-	1.3	9.5	2.1	4.9
Max FRP flux density (kW m^{-2})	8.3	10.1	2.0	-	7.1	18.7	7.3	6.8
Total FRE (MJ)	3.2	2.1 (0.6)	2.2	-	1.2	2.0 (0.6)	1.4	1.3 (0.3)
Total FRED (MJ m^{-2})	0.267	0.175 (0.05)	0.144	-	0.103	0.17 (0.05)	0.107	0.108 (0.025)
Total area overlap (m^2)	12	12	16	-	12	12	16	16

Continuation of Table 2.

	Nadir LWIR Plot					
	L1G plot 1	L1G plot 2	L2G plot 1	L2G plot 2	L2F plot 2	L2F plot 3
Mean (SD) FRP (kW)	15 (26)	27 (24)	23 (29)	14 (23)	33 (47)	41 (55)
Max FRP (kW)	84	70	90	83	156	208
Mean FRP flux density (kW m^{-2})	3.7	2.3	1.4	3.4	2.1	2.6
Max FRP flux density (kW m^{-2})	20.9	5.5	5.6	20.8	9.7	13
Total FRE (MJ)	1.3	3.2	3.2	2.1	12	12.1
Total FRED (MJ m^{-2})	0.325	0.267	0.2	0.525	0.75	0.756
Total area measured (m^2)	4	12	16	4	16	16

Fig. 1. (*a*) Tripod system and (*b*) boom lift used to collected nadir and oblique LWIR thermographic measurements, respectively, of surface wildland fires.

Fig. 2. (*a*) Snapshot of nadir LWIR imagery versus (*b*) a color digital photograph of a surface fire (L2F HIP 3). Note the transparency of smoke in the LWIR imagery and the detection of thermal signatures of both flaming and smoldering combustion. The metal targets (in *b*) are used for post processing and are positioned 1 m apart around the SHIP perimeter. Color legend for the LWIR image is in °C.

Fig. 3. Total FRED (GJ ha^{-1}) across oblique LWIR imagery. The burn block is a subset of the burn unit, or entire area burned. Indicated wind direction is approximate. Fires were lit outside the unit on the upwind side of the unit and allowed to burn through the burn block and beyond. The boom lift locations indicate where the oblique LWIR camera was positioned 25 m above ground level.

Fig. 4. Nadir FLIR fire radiative power (FRP) measurements within 4 m x 4 m SHIPs in four of the small burn blocks.

Fig. 5. Nadir FLIR FRP measurements within 4 m x 4 m SHIPs in the large burn units. Units labled L1G and L2G were nonforest, unit L2F was forested. Note the longer residence time and greater energy released in the forested SHIPs.

Fig. 6. Temporal FRP (MW) at 1 Hz collected across the entire fire perimeter of each small nonforested burn block using the oblique LWIR imagery. Fluctuations in FRP are in response to changes in fuels, wind patterns and velocity as well as fire line depth and extent within each block. Time relates to the amount of time between ignition and the fire leaving the camera's field of view and/or reaching the downwind control line. Note the difference in scale of FRP and time between graphs. Graphs are labeled by block names.

Fig. 7. Chosen oblique LWIR images of a small burn block (S5) representing the moving fire front. At one minute, the fire is still moving along the original ignition line. By three minutes, the fire develops flanks. Differences in the width of the flaming front illustrate changes in wind velocity and direction. Image resolution: 1 m x 1 m. Approximate area in figure display: 2 ha (100 m x 200 m).

Fig. 8. Cross-scale comparison of fire radiative power measured from the oblique (rectified) and nadir cameras within the same area (the 4 m x 4 m nadir FLIR field-of-view) within the S5 block. Data are represented as (*a*) FRP (kW) at each timestamp, (*b*) FRP flux density (kW m^{-2}) at each timestamp, and (*c*) cumulative FRE released from fire (kJ). Total FRE released from the fire within the SHIPS was 2.1 (0.6 sd) and 3.2 MJ for the oblique and nadir imagery, respectively. The x-axis represents relative time from initial fire detection in the 4m x 4m SHIPs. FRP for the oblique LWIR is represented as mean and standard deviation of 20 overlapping oblique 1-m^2 pixels within the 12-m^2 SHIPs.

Fig. 9. Nadir and oblique imagery comparison of FRP in small burn blocks (*a*) S8 and (*b*) S9. Nadir and oblique data were collected at approximately 1 Hz and 0.17 Hz respectively within each block. Data corresponds to an overlap in area of 12 m^2 and 16 m^2 for (*a*) and (*b*), respectively. Note the early fluctuations in FRP in S8, where camera movement on the oblique platform caused temporal and spatial shifts in data collection, compared to S9, where there was little camera movement.

Fig. 10. Example of spatially explicit FRE estimated with the nadir imagery in one forested (L2F HIP 3) and nonforested unit (S5). Note the difference in scale and patchiness of FRED between units. The scale bar is in FRED (J m^{-2}).

Fig. 11. The modeled spatial autocorrelation of FRE and residence time within one nonforested (S5) and one forested SHIP (L2F HIP3).

Figure 1.

Figure 2.

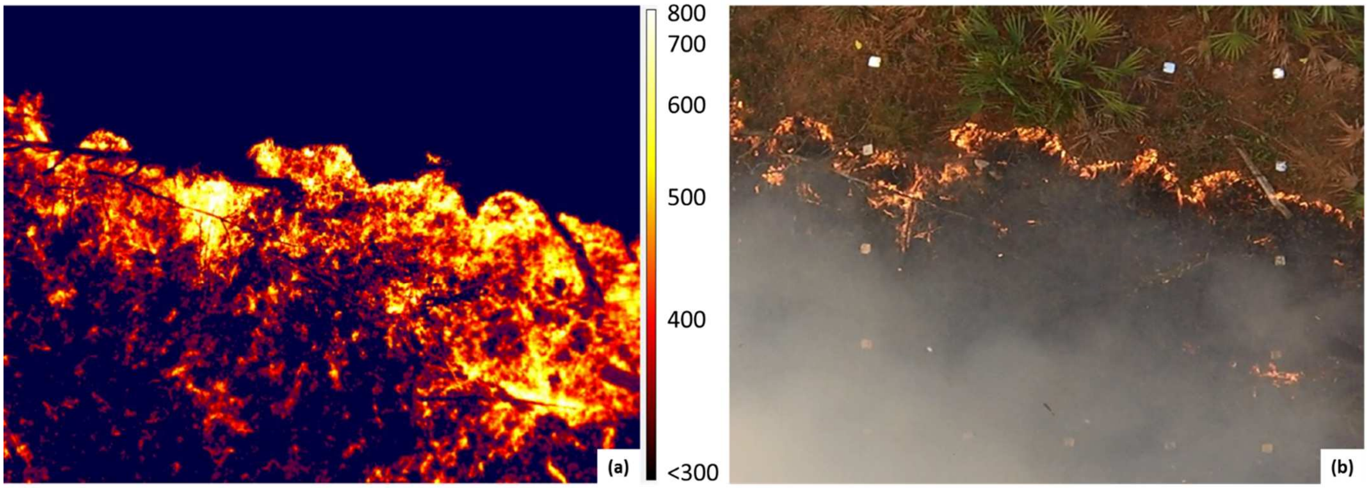

Figure 3.

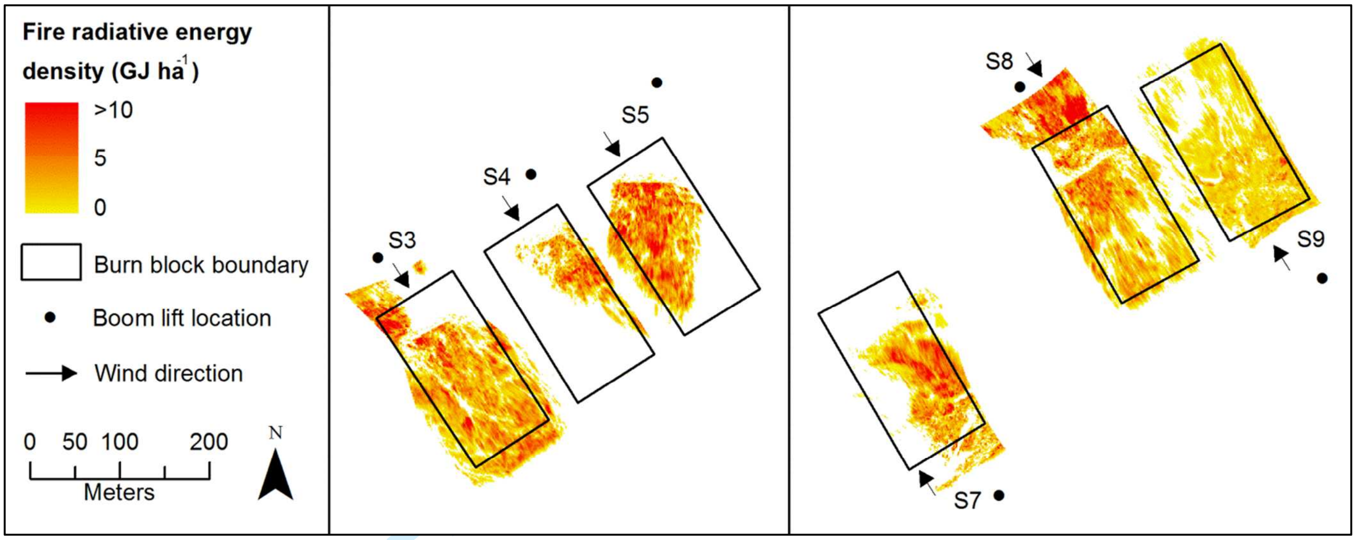
Fire radiative energy density (GJ ha-1)
>10
5
0
Burn block boundary
Boom lift location
Wind direction
0 50 100 200
Meters
N
S3
S4
S5
S7
S8
S9

Figure 4.

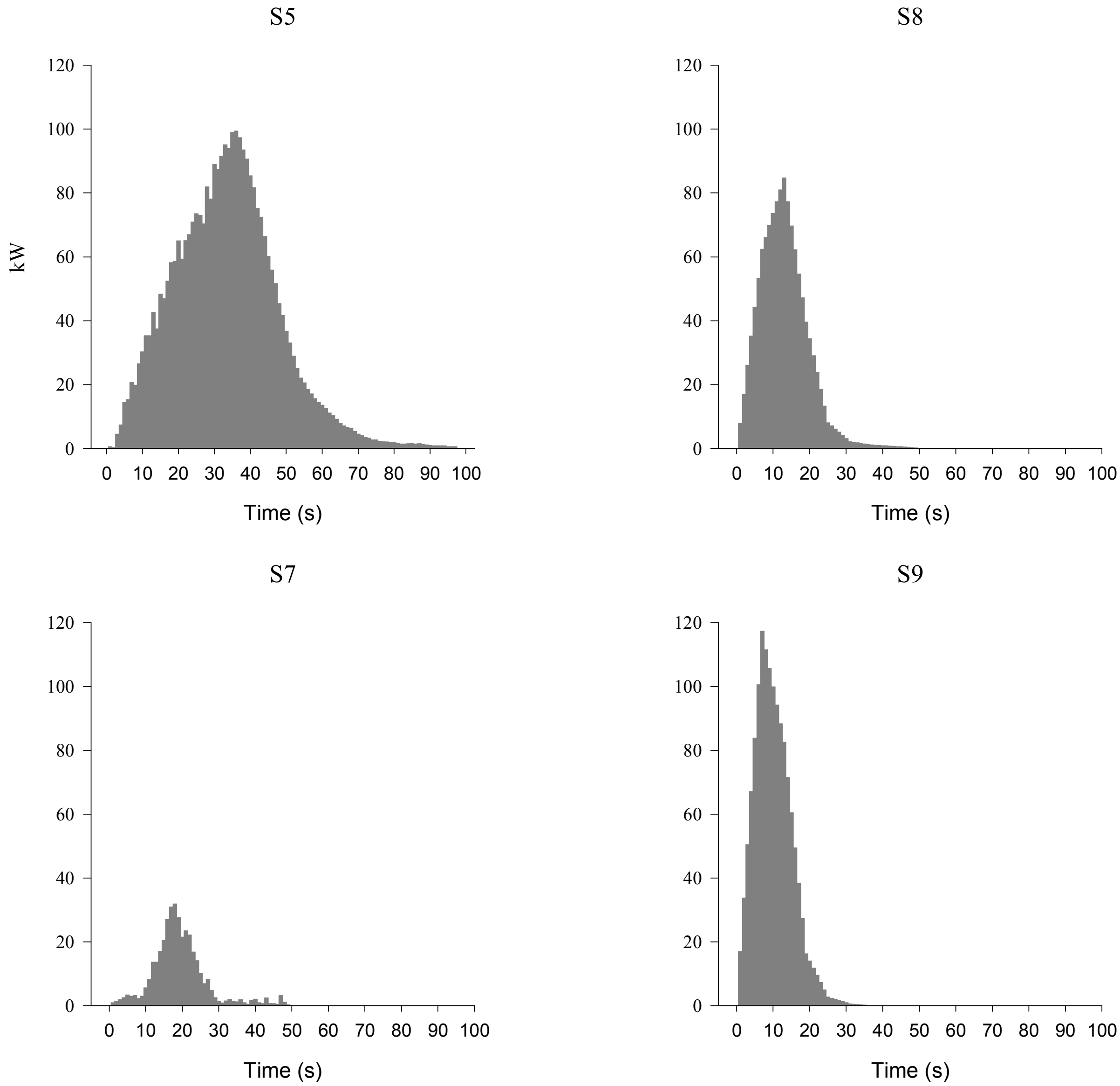
S5
S8
S7
S9
kW
Time (s)
0
20
40
60
80
100
120
0 10 20 30 40 50 60 70 80 90 100

563 Figure 5.

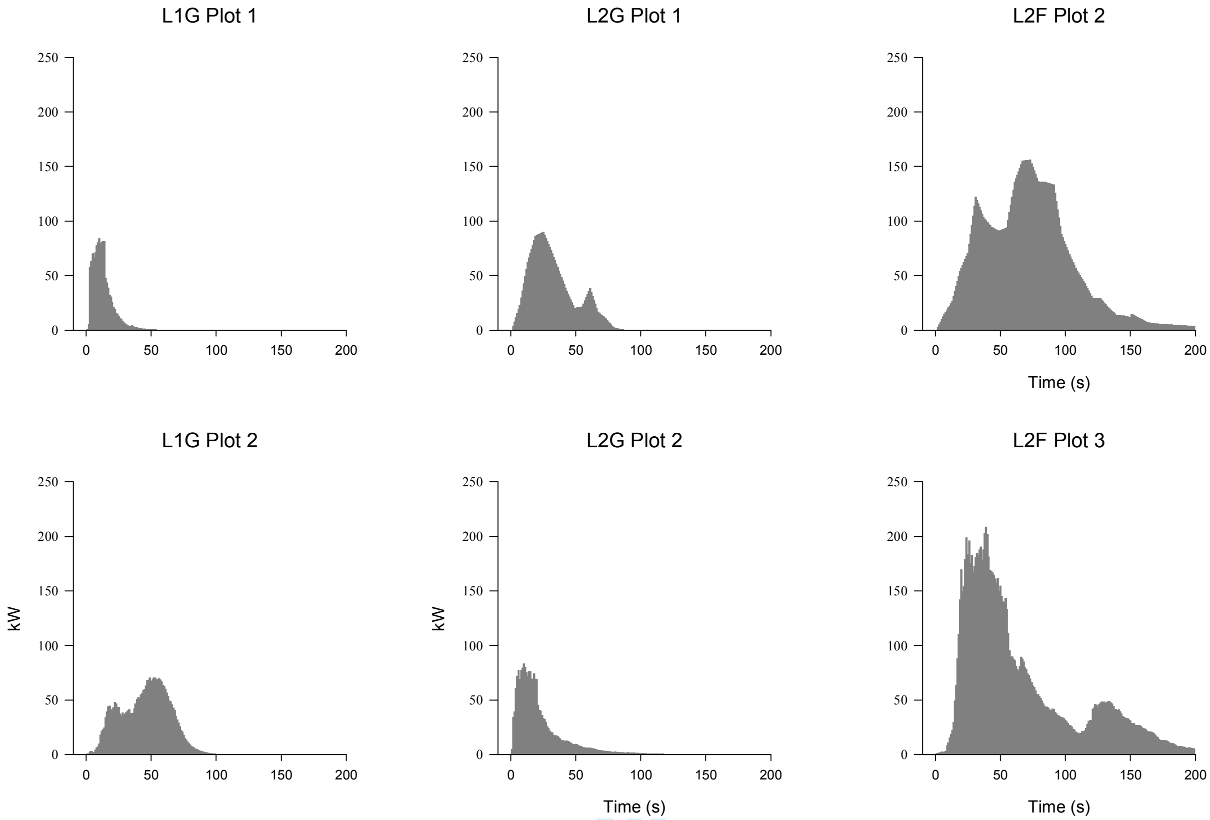

564

565

Figure 6.

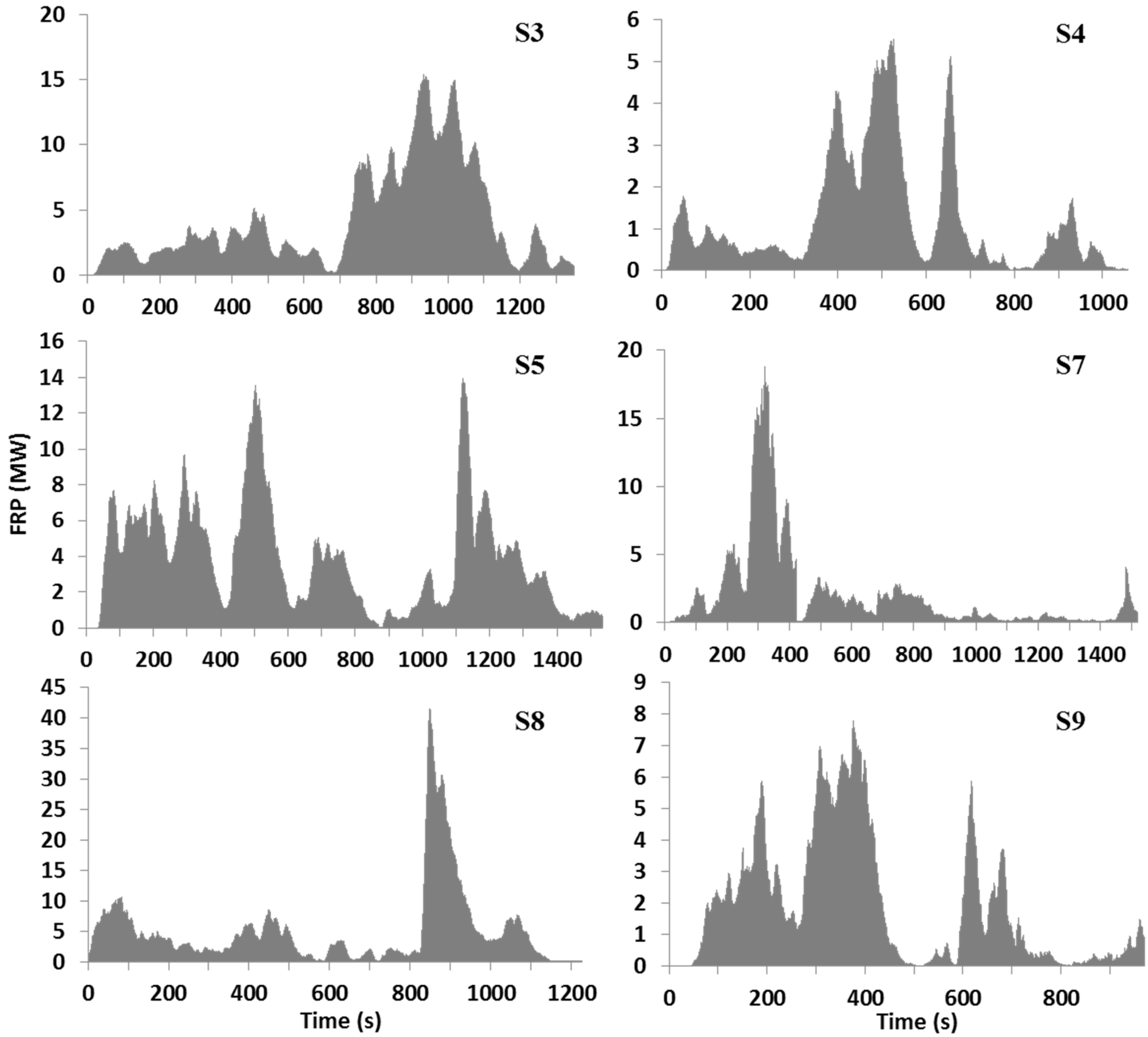

Figure 7.

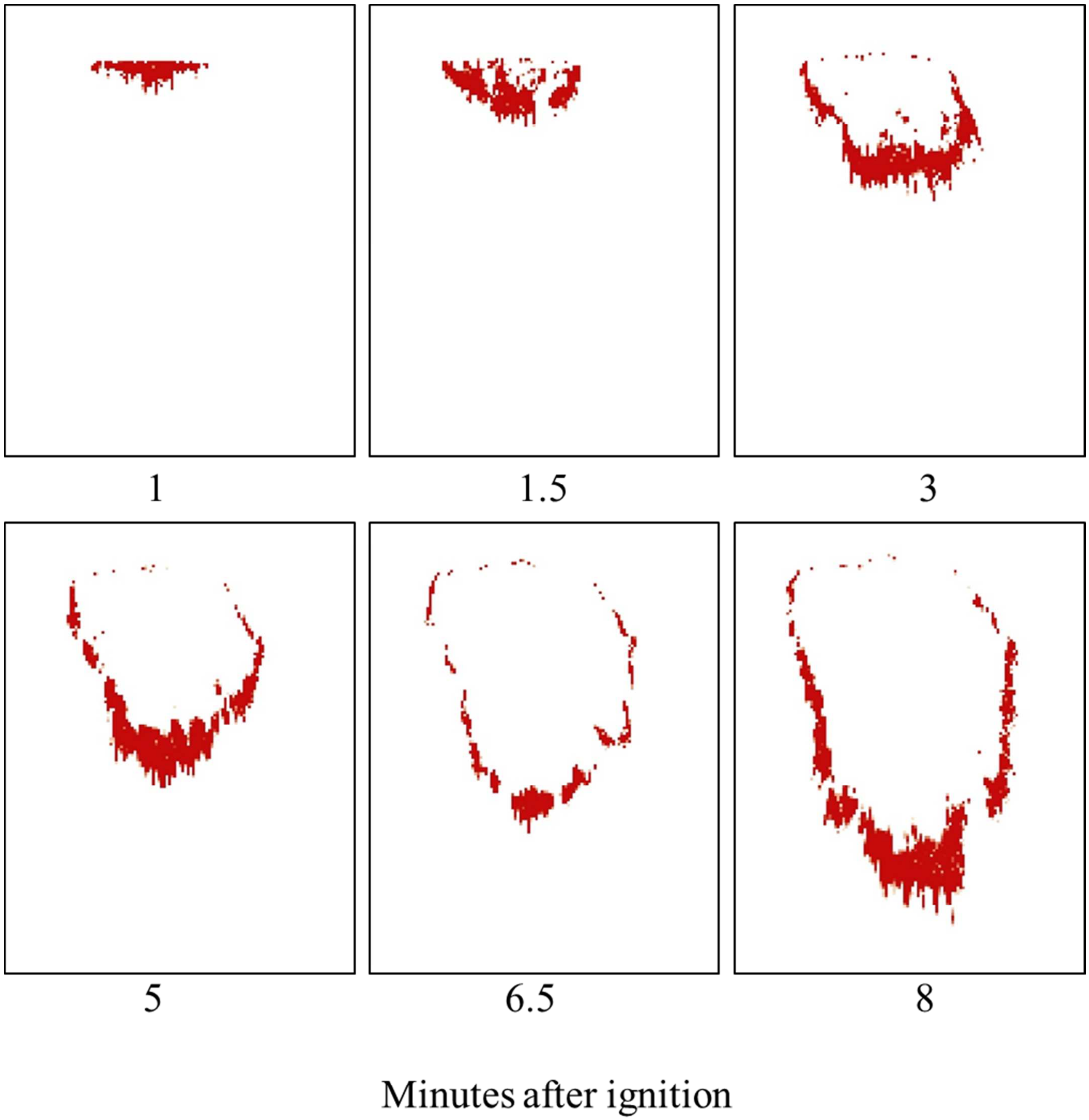

Figure 8.

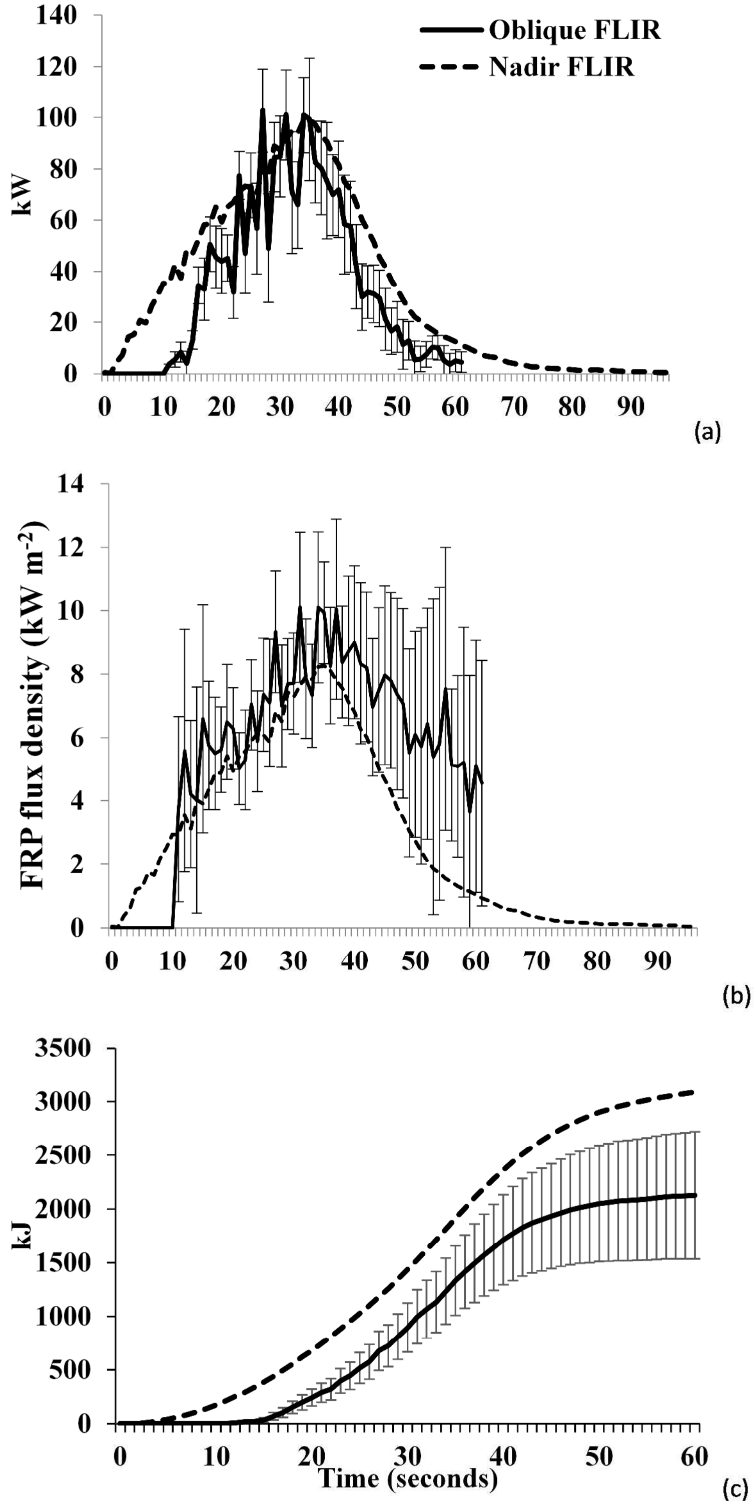
Oblique FLIR
Nadir FLIR
kW
140
120
100
80
60
40
20
0
0 10 20 30 40 50 60 70 80 90
(a)
FRP flux density (kW m-2)
14
12
10
8
6
4
2
0
0 10 20 30 40 50 60 70 80 90
(b)
kJ
3500
3000
2500
2000
1500
1000
500
0
0 10 20 30 40 50 60
Time (seconds)
(c)

Figure 9.

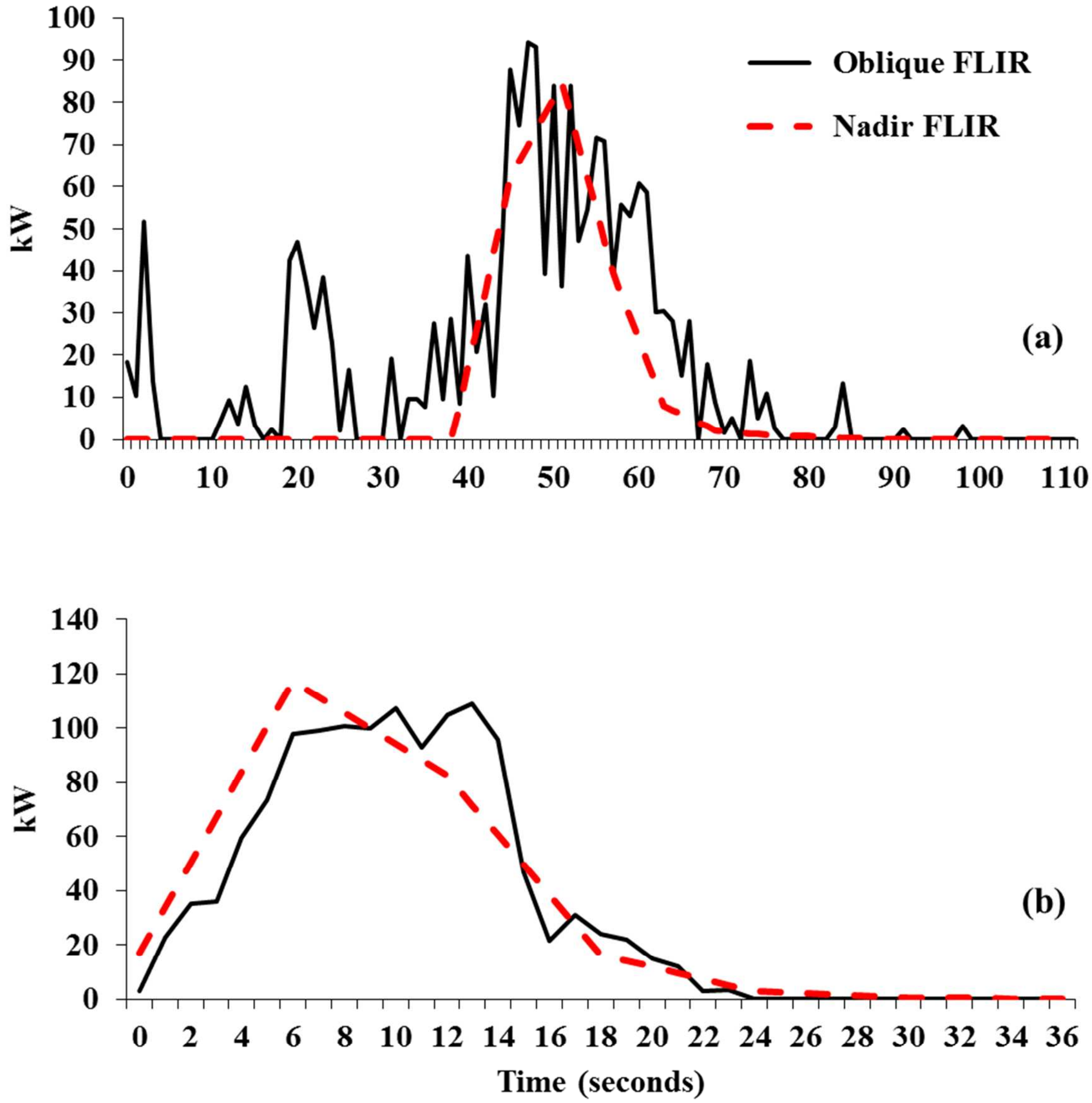

Figure 10.

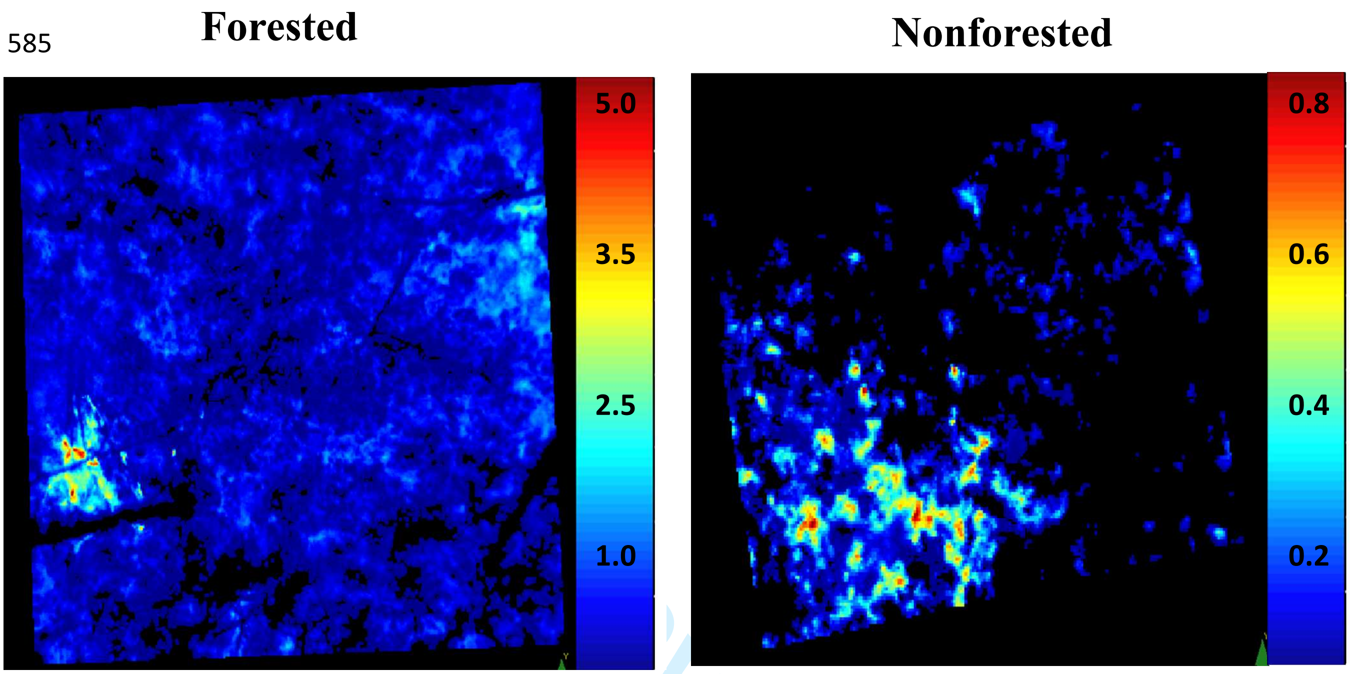

586 Figure 11.

587